

# Constraints on perfect fluid and scalar field dark energy models from future redshift surveys

L. Amendola<sup>1</sup>, C. Quercellini<sup>1,2,3</sup> & E. Giallongo<sup>1</sup>

<sup>1</sup>INAF/Osservatorio Astronomico di Roma

*Via Frascati 33, 00040 Monteporzio Catone (Roma), Italy*

<sup>2</sup>Università di Roma Tor Vergata, Dip. di Fisica,

*Via della Ricerca Scientifica 1, 00133 Roma, Italy*

<sup>3</sup>University of Oxford, Keble Road, OX1 3RH, Oxford, UK

Accepted ...., Received

## ABSTRACT

We discuss the constraints that future photometric and spectroscopic redshift surveys can put on dark energy through the baryon oscillations of the power spectrum. We model the dark energy either with a perfect fluid or a scalar field and take into account the information contained in the linear growth function. We show that the growth function helps to break the degeneracy in the dark energy parameters and reduce the errors on  $w_0, w_1$  roughly by 30% making more appealing multicolor surveys based on photometric redshifts. We find that a 200 deg<sup>2</sup> spectroscopic survey reaching  $z \approx 3$  can constrain  $w_0, w_1$  to within  $\Delta w_0 = 0.21, \Delta w_1 = 0.26$  and to  $\Delta w_0 = 0.39, \Delta w_1 = 0.54$  using photometric redshifts with absolute uncertainty of 0.02. In the scalar field case we show that the slope  $n$  of the inverse power-law potential for dark energy can be constrained to  $\Delta n = 0.26$  (spectroscopic redshifts) or  $\Delta n = 0.40$  (photometric redshifts), i.e. better than with future ground-based supernovae surveys or CMB data.

**Key words:**

## 1 INTRODUCTION

Dark energy is the most elusive component of the universe: it is dark, it does not cluster and, in most models, it is subdominant in cosmic history until recently. On the other hand, it is

also the most pervasive component, in that it affects background expansion, linear dynamics and possibly non-linear as well.

The characterization of DE has been so far based almost uniquely on background tests at rather low redshifts ( $z < 1$ : Riess et al. 1998, Perlmutter et al. 1999, Tonry et al. 2003, Riess et al. 2004) or very large redshifts ( $z \approx 1000$ : e.g. Netterfield et al. 2002, Halverson et al. 2002, Lee et al. 2002, Bennett et al. 2003), although tests at intermediate redshifts based on strong lensing have also appeared (Soucail, Kneib & Gole 2004). These tests are based essentially on estimations of luminosity  $D_L$  or angular-diameter distances  $D(z)$ , i.e. on integrals of the Hubble function  $H(z)$  which, in turn, contains an integral of the equation of state. If we aim at making real progress it is then necessary to cross this information with probes at intermediate  $z$  and with other observables such as the linear growth function  $G(z)$ . The goal of this paper is to show how future observations of large scale structure (LSS) at  $z$  up to 3 can set interesting limits on models of DE taking advantage of the complementarity between  $H$ ,  $D$  and  $G$ .

The method we use is based on recent proposals (Linder 2003, Blake & Glazebrook 2003, Seo & Eisenstein 2003) to exploit the baryon oscillations in the power spectrum as a standard ruler calibrated through CMB acoustic peaks. In particular, Blake & Glazebrook (2003) and Seo & Eisenstein (2003; hereinafter SE) have shown the feasibility of large (100 to 1000 square degrees) spectroscopic surveys at  $z \approx 1$  and  $z \approx 3$  to put stringent limits to the equation of state  $w(z)$  and its derivative. SE have also shown that the redshift error introduced by a photometric survey (with a relative error on  $1+z$  of 1%) could be compensated only by a 20-fold increase of the sampled volume.

This paper has a threefold motivation. First, we extend the Fisher matrix method by taking into account the information on the DE evolution contained in the growth factor  $G$  at various redshifts. While SE marginalized over  $G$ , we find that its marked dependence on the cosmological parameters, especially on  $\Omega_m$ , associated with its different direction of degeneracy, are helpful in narrowing down the constraints. Secondly, we extend the analysis to a scalar field model of DE with inverse power-law potential (Ratra & Peebles 1988), based on the inverse power-law potential: this allows us to evaluate the growth function without further assumptions and to exploit the properties of tracking solutions (Steinhardt et al. 1999). Third, we pay special attention to the possibility of testing DE with a photometric redshift survey. Indeed the effect of the growth factor in reducing the confidence regions of the cosmological parameters makes more appealing the use of photometric redshift surveys to show any possible redshift evolution of the DE. We explore the constraints derived on the cosmological parameters from relatively wide multicolor surveys where the absolute redshift uncertainty keeps almost constant around  $\delta z = 0.02 - 0.04$  in the redshift range  $z = 0 - 3.5$ . Such surveys can be realized with the current wide field imagers on 4-8m class telescopes.

Finally, it is interesting to speculate on another aspect of the method. The baryon oscillation scale measures the angular-diameter distance  $D(z)$  while the SNIa method observes the luminosity distance. As remarked recently by Bassett & Kunz (2003) the two quantities are related in a trivial way only in standard cosmologies: new physics like photon decay can lead to an observable breaking of their “reciprocity” relation. A photometric survey can be adapted to the scope since the degradation of the error in  $D(z)$  due to the redshift smearing is relatively reduced (with respect to the error in  $H(z)$ ), as it will be shown below.

## 2 FISHER MATRIX METHOD

The method proposed in SE is based on the Fisher matrix, an approximation to the likelihood function that provides under some conditions the minimal errors that a given experiment may attain (Eisenstein, Hu & Tegmark 1999, EHT). Here we review the method adopting the notation of SE, to which we refer for further details. Our starting point is a cosmological model that predicts the evolution of the Hubble parameter,  $H(z)$ , and the growth of linear perturbations,  $G(z)$ . From  $H(z)$  we can estimate the angular-diameter distance in flat space as (we put  $c = 1$ )

$$D(z) = (1+z)^{-1} \int_0^z \frac{dz'}{H(z')} . \quad (1)$$

Let us choose a reference cosmology, denoted by a subscript  $r$ , for instance  $\Lambda CDM$ , and calculate the matter power spectrum in real space at  $z = 0$ ,  $P_{0r}(k_r)$ . Then the predicted observable galaxy power spectrum in a different cosmology  $C$  (no subscript) at  $z$  in redshift space is

$$P_{obs}(z; k_r, \mu_r) = P_s(z) + \frac{D_r^2(z)H(z)G^2(z)}{D^2(z)H_r(z)} \frac{\Omega_m^{1.2}(z)}{\beta^2(z)} (1 + \beta\mu^2)^2 P_{0r}(k) , \quad (2)$$

where  $k$  is the wavenumber modulus and  $\mu$  its direction cosine. Several comments will clarify the meaning of this equation.  $P_s(z)$  is a scale-independent offset due to incomplete removal of shot-noise. The factor  $(D^2/H)/(D_r^2/H_r)$  takes into account the difference in comoving volume between the two cosmologies. The factor  $(1 + \beta\mu^2)^2$  is the redshift distortion.  $G(z)$  is the growth factor of the linear density contrast  $\delta_m$ ,

$$G(z) = \delta_m(z)/\delta_0 , \quad (3)$$

where  $\delta_0$  is the present density contrast (and therefore  $G(z)$  is normalized to unity today). The density parameter  $\Omega_m(z)$  depends on the cosmology. In flat-space  $\Lambda CDM$  it is given by

$$\Omega_m(z) = \frac{\Omega_{m0}(1+z)^3}{\Omega_{m0}(1+z)^3 + 1 - \Omega_{m0}} , \quad (4)$$

and it is therefore parametrized by the present density parameter  $\Omega_{m0}$ . The bias parameter  $\beta(z) = \Omega_m^{0.6}(z)/b(z)$  (assumed scale-independent) is evaluated for the reference cosmology using the formula

$$\sigma_{8,g} = \beta(z)^{-1} \Omega_m^{0.6}(z) \sigma_{8,m}(z) \sqrt{1 + \frac{2\beta(z)}{3} + \frac{\beta^2(z)}{5}} , \quad (5)$$

where  $\sigma_8$  is the variance in spherical cells of 8 Mpc/ $h$  for galaxies (subscript  $g$ ) or matter ( $m$ ) (notice that the variance  $\sigma_8$  is calculated using the power spectrum averaged over  $\mu$ ). Finally, we can include a redshift error by rescaling the power spectrum

$$P = P_{obs} e^{-k^2 \mu^2 \sigma_r^2} , \quad (6)$$

where

$$\sigma_r = (\delta z)/H(z) , \quad (7)$$

is the absolute error in distance and  $\delta z$  the absolute error in redshift.

We need also the relation between the line-of-sight and transverse wavenumbers  $k_\perp, k_\parallel$  and the reference values:

$$k_{r\perp} = k_\perp D/D_r, \quad (8)$$

$$k_{r\parallel} = k_\parallel H_r/H. \quad (9)$$

From these relations we derive the relation between the wavenumber modulus  $k$  and the direction cosine  $\mu = \mathbf{k} \cdot \mathbf{r}/k$  in the reference cosmology and in the cosmology  $C$

$$k = R k_r, \quad (10)$$

$$\mu = \frac{H \mu_r}{H_r R}, \quad (11)$$

where

$$R = \frac{\sqrt{D^2 H^2 \mu_r^2 - D_r^2 H_r^2 (\mu_r^2 - 1)}}{D H_r}. \quad (12)$$

The observed power spectrum in a given redshift bin  $z_0$  depends therefore on a number of parameters, denoted collectively  $p_i$ , such as  $\Omega_{m0}, G(z_0), H(z_0)$  etc, as detailed in Table I. The redshift-dependent parameters ( $P_s, H, G, D, \beta$ ) are assumed to be approximately constant in each redshift bin. Then we calculate, numerically or analytically, the derivatives

$$\left( \frac{\partial \log P}{\partial p_i} \right)_{ref}. \quad (13)$$

Finally, the Fisher matrix is (Tegmark 1997)

$$F_{ij} = \frac{1}{8\pi^2} \int_{-1}^1 \int_{k_{min}}^{k_{max}} \left( \frac{\partial \log P}{\partial p_i} \frac{\partial \log P}{\partial p_j} \right)_{ref} V_{eff}(k, \mu) k^2 dk d\mu, \quad (14)$$

where

$$V_{eff}(k, \mu) = \left[ \frac{n P(k, \mu)}{n P(k, \mu) + 1} \right]^2 V_{survey}, \quad (15)$$

$n$  being the number density of galaxies.

In the following we will use also the CMB Fisher matrix (Seljak 1996, EHT)

$$F_{ij,CMB} = \sum_{\ell} \sum_{X,Y} \frac{\partial C_{X,\ell}}{\partial p_i} (Cov_{\ell})_{XY}^{-1} \frac{\partial C_{Y,\ell}}{\partial p_j}, \quad (16)$$

where  $C_{X,\ell}$  is the multipole spectrum of the component  $X$ , and  $X = T, E, B, C$  denote the temperature  $T$ ,  $E$  and  $B$  polarization, and the cross-correlation  $TE$ , respectively, with covariance matrix  $(Cov_{\ell})_{XY}$ . We adopt the same specifications used in EHT and in SE, corresponding to an experiment similar to the Planck satellite. The spectra have been obtained with the Boltzmann code Cmbfast (Seljak & Zaldarriaga 1996). Once we have the Fisher matrices for all data we sum to obtain the total combined matrix

$$F_{ij} = F_{ij,CMB} + \sum F_{ij,survey}. \quad (17)$$

The independent parameters to be included in the Fisher matrix are listed in Table I.

Table I. Parameters

$P_0(k)$		
1	reduced total matter	$\omega_m \equiv \Omega_{m0}h^2$
2	reduced baryon dens.	$\omega_b \equiv \Omega_{b0}h^2$
3	optical thickness	$\tau$
4	primord. fluct. slope	$n_s$
5	total matter dens.	$\Omega_{m0}$
For each survey at $z$		
6	shot noise	$P_s$
7	ang-diam. distance	$\log D$
8	Hubble param.	$\log H$
9	growth function	$\log G$
10	bias	$\log \beta$
additional CMB parameters		
11	decoupling ang.-diam. dist.	$\log D$
12	tensor-to-scalar ratio	$T/S$
13	$C_\ell$ normalization	$\log A_s$

The main difference with respect to the method of SE is that we exploit the information contained in the growth function. As it will be seen below, this information is of great help in reducing the bounds on the DE parameters, for two concurrent reasons: first,  $G$  has a marked dependence upon the cosmological parameters, i.e.  $d \log G/d\Omega_{m0}$  is at  $z > 1$  as large as  $d \log D/d\Omega_{m0}$  and quite larger than  $d \log H/d\Omega_{m0}$  (see Fig. 1); second, the parameter degeneracy in  $G(z)$  has a slightly different direction with respect to the degeneracies in  $H$  and  $D$  (see the discussion in Cooray, Huterer & Baumann 2004 ).

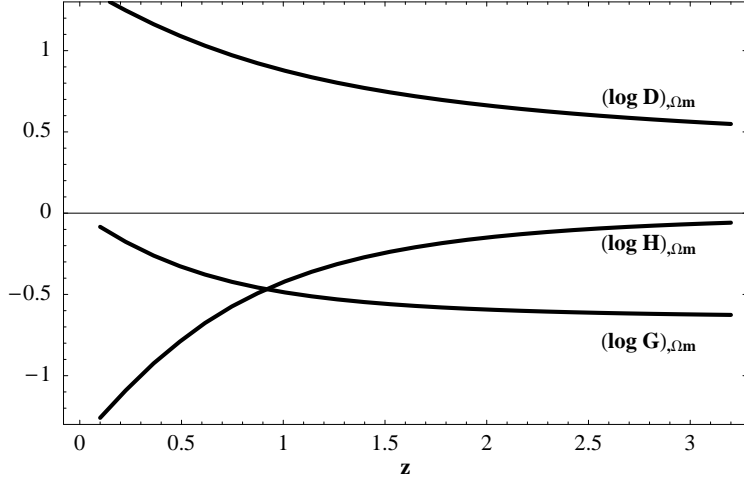


**Figure 1.** Derivatives  $\partial \log X / \partial \Omega_{m0}$  as function of  $z$ , where  $X = H, D, G$ .

Unless differently specified, the reference cosmology is  $\Lambda CDM$  with the same parameters as in SE,  $\Omega_m = 0.35$ ,  $h = 0.65$ ,  $\omega_b = 0.021$ ,  $\tau = 0.05$ ,  $n_s = 1$ ,  $T/S = 0$ ,  $P_s = 0$ .

### 3 THE SURVEYS

One of the main aim of the paper is to show how it is possible to build, using deep and wide multicolor surveys, a photometric redshift sample of galaxies suitable for the analysis of the galaxy power spectrum as a function of redshift. Previous analyses reached two main conclusions about the possible strategy. First of all spectroscopic surveys are clearly favorite with respect to photometric surveys because any uncertainty  $> 1\%$  in the photometric redshifts increases the uncertainty on  $H(z)$  at  $z > 0.5$  to  $> 10\%$ , for surveys covering areas of  $100 - 1000$  deg $^2$ . Second, the relatively bright magnitude limit needed to keep a high completeness level in the spectroscopic follow up implies a low number density of sources per unit area. Large survey areas are hence needed to guarantee adequate total number of objects. Here we show that it is possible to envisage a photometric redshift survey with adequate depth and limited area of the sky at  $z = 0.5 - 1$  and at  $z = 2.7 - 3.5$  that can provide constraints on the redshift dependence of the DE equation of state which are competitive with those obtained from SNIa and CMB in the foreseeable future.

To measure the redshift evolution of  $H(z)$  and of the angular diameter it is important to analyse the power spectrum in a wide redshift interval with specific sampling at  $z = 0.5 - 1$  and especially at  $z = 3$  where the linear regime of galaxy clustering extends to smaller physical scales allowing the analysis of acoustic oscillations to higher frequencies in the range  $0.1 < k < 0.5 \text{ h Mpc}^{-1}$ . What is important is the estimate of the characteristic wavelength of the acoustic oscillations,  $k_A = 2\pi/s$  which is connected with sound horizon  $s$  at recombination. For our standard  $\Lambda$ CDM model  $k_A \simeq 0.06 \text{ h Mpc}^{-1}$ . It is important to emphasize that local surveys could probe only the first peak at  $k \simeq 0.075 \text{ h Mpc}^{-1}$ . Thus, an appropriate comparison with the CMB power spectrum requires higher frequencies and consequently high redshift surveys, in particular at  $z = 3$ .

Indeed, large scale galaxy surveys at  $z \geq 3$  could in principle be built in a straightforward way using the standard multicolor dropout technique which exploits the detection in the galaxy spectra of the UV Lyman absorption due to the local ISM in the galaxy and in the intergalactic medium present along the line of sight. At  $z = 2.5 - 3.5$  the Lyman series absorption progressively enters the UV filter causing a reddening in the U-R galaxy color. At  $z = 3.5 - 4.5$  the dropout shift in the blue causing a reddening in the B-R galaxy color and so on. Spectroscopic confirmation has provided a relatively high success rate 75% (Steidel et al. 1996, 1998) although in practice it is difficult to obtain a high completeness level in the magnitude interval  $R = 24 - 25.5$ , which is the present limit for systematic spectroscopic follow up at 10m class telescopes. A survey completeness level of 90% could be reached more easily at  $R < 24.5$  but with a surface density of  $\sim 0.3 \text{ arcmin}^{-2}$  at  $z = 2.5 - 3.5$ . The color selection of the sample requires very deep exposures in the UV band implying efficient UV imagers at 8-10m class telescopes to cover a large area in a short time. Surveys at  $z > 3.5$  which use a B-dropout technique can avoid high UV efficiency but the surface density of objects at the spectroscopic limit of  $I \sim 25$  is only  $\sim 0.1 \text{ arcmin}^{-2}$ . In other words galaxies at  $z \sim 4 - 5$  are rarer and fainter. With these considerations, surveys at  $z \sim 3$  down to a magnitude limit of  $R \sim 25$  are the best compromise for the study of large scale structures at high redshift provided that efficient wide field imagers with high UV efficiency are used. The Large Binocular Camera in construction at the prime focus of the Large Binocular Telescope is an ideal imager to this aim (Pedichini et al. 2003).

It is well known from the previous studies that there are two sources of statistical error in the power spectrum estimate. The sample variance, due to the number of wavelength bins, depends on the survey volume and on the scale of the selected acoustic peak in the linear regime (e.g. Peacock & West 1992; Blake & Glazebrook 2003):

$$\left(\frac{\sigma_P}{P}\right)^2 = 2 \times \frac{(2\pi)^3}{V} \times \frac{1}{4\pi k^2 \Delta k}.$$

The shot noise is the other source of noise. For a fixed volume it decreases with increasing  $nP > 1$ , where  $n$  is the comoving galaxy number density. In practice it is possible to show that the decrease of the shot noise saturates for  $nP \gg 1$  and values in the range  $1 < nP < 5$  are more appropriate (SE).

To reach at least the second peak at  $k = 0.135 \text{ h Mpc}^{-1}$  it has been shown that adopting  $\Delta k = k_A/4 = 0.015 \text{ h Mpc}^{-1}$  to ensure an adequate wavelength sampling, a value  $\frac{\sigma_P}{P} = 0.02$  is needed as the fractional height of the peak is about 4% (Blake & Glazebrook 2003). This

requires that volumes of the order of  $3.6 \times 10^8 h^{-3} \text{ Mpc}^3$  should be mapped at  $z = 0.5 - 1$  and at  $z = 3$ . Since the volume per square degree is  $V \simeq 3.5 \times 10^6 h^{-3} \text{ Mpc}^3 \text{ deg}^{-2}$  at  $z = 2.5 - 3.5$  and  $V = 1.7 \times 10^6 \text{ Mpc}^3 \text{ deg}^{-2}$  at  $z = 0.5 - 1.3$  this implies surveys at least of the order of  $100 - 200 \text{ deg}^2$  at  $z \sim 3$  and  $z \sim 1$ , respectively.

Concerning the shot noise, the condition of  $1 < nP < 5$  implies  $n \sim 4 - 20 \times 10^{-4} \sigma_{8,g}^2 h^3 \text{ Mpc}^{-3}$  respectively, given  $P \approx 2500 \sigma_{8,g}^2 (\text{Mpc}/h)^3$  at  $k = 0.2 h/\text{Mpc}$ .

At  $z = 3$ , a photometric redshift survey down to the magnitude limit of  $R \leq 25$  gives a total number density in the range  $z = 2.7 - 3.5$  of  $n \sim 2 \times 10^{-3} h^3 \text{ Mpc}^{-3}$  after integration over the UV Schechter luminosity function of Poli et al. (2001).

At  $z = 1$ , the same photometric survey at  $R \leq 25$  in the range  $z = 0.5 - 1$  would give a total number density of  $\sim 4.5 \times 10^{-2} h^3 \text{ Mpc}^{-3}$  as obtained from the blue luminosity function of Poli et al. (2003). For sake of comparison, we adopt the same redshift binning at  $z \approx 1$  as SE.

Detailed densities and volumes for the basic surveys of area  $100 \text{ deg}^2$  are shown in Table II in the same redshift intervals used by SE (except we restrict conservatively the deepest survey to  $z > 2.7$  instead of  $z > 2.5$ ). We will present results also for larger surveys, corresponding to areas of  $200 \text{ deg}^2$  and  $1000 \text{ deg}^2$  respectively, and with sparser surveys at  $z \approx 1$ , adopting a density 10 times smaller as that quoted in Table II. The absolute error in redshift is taken to be either zero (spectroscopic survey) or  $\delta z = 0.02$  and  $\delta z = 0.04$  (photometric surveys). Finally, we also include results for a *hybrid* survey, i.e. a photometric survey with  $\delta z = 0.02$  at  $z \approx 1$  combined with a spectroscopic at  $z \approx 3$ . This choice depends on the fact that multi object spectroscopy of a complete color selected sample of Lyman break galaxies at  $z = 3$  is able to give more stringent constraints on the cosmological parameters (see Fig. 3) than a similar survey at  $z \approx 1$  in the same area. Moreover a spectroscopic survey at  $z \approx 3$  appears also more efficient in terms of multiplexing and completeness level if the magnitude limit is  $R \leq 25$ , corresponding to a surface density  $\leq 1 \text{ arcmin}^2$ . At  $z = 1$ , on the contrary, the average surface density even at the relatively shallow limit  $R = 23$  is already of the order of  $8 \text{ arcmin}^2$  implying a multiplexing of more than 460 targets in a field of e.g.  $7 \times 8 \text{ arcmin}^2$  to be compared with the multiplexing capabilities of recent instruments at 8m class telescopes like VIMOS at ESO/VLT where only 150 targets can be observed in a single exposure in the same area.

Table II. Surveys

$z$	$V_s$ (Gpc $^3$ )	$n$
0.5 – 0.7	0.030	$6.9 \cdot 10^{-2}$
0.7 – 0.9	0.040	$4.2 \cdot 10^{-2}$
0.9 – 1.1	0.050	$3.1 \cdot 10^{-2}$
1.1 – 1.3	0.057	$2.4 \cdot 10^{-2}$
2.7 – 3.5	0.27	$2 \cdot 10^{-3}$

As in SE, to these surveys we add data from SDSS (Eisenstein et al. 2001). The SDSS data is always considered spectroscopic.

Redshift errors of the order of 1-2% from photometric surveys are demanding but still reachable if the photometric accuracy is  $\delta m \simeq 0.02$  and if a good wavelength coverage and sampling is guaranteed (see e.g. Wolf et al. 2001). This requires broad and intermediate band imaging on wide field imagers at 8m class telescopes like Suprim-Cam at the SUBARU or the upcoming Large Binocular Camera at the Large Binocular Telescope (LBT). In particular the use of intermediate band filters in the optical range can be important to ensure the required redshift accuracy in the specific redshift intervals  $z \sim 1$  and  $z \sim 3$ . In the redshift interval  $z = 1.5 – 2.5$  near infrared imaging is needed on wide areas but this requires a new generation of NIR instruments.

To the redshift surveys we add CMB data, adopting the same Planck-like specifications of SE and EHT. Finally, we evaluate SN constraints from surveys that reproduce approximately near future catalogs from ground-based observations: 400 SNIa distributed uniformly in redshift between  $z = 0$  and  $z = 1.5$ , with magnitude errors  $\Delta m = 0.25$  and the same stretch factor correction as in the sample of Perlmutter et al. (1999). We marginalize over the  $H$ -dependent magnitude  $\mathcal{M}$  and over the stretch factor. These SN likelihood functions are therefore completely independent of the Hubble constant determination. We also compare with SN likelihood contours obtained assuming an independent 10% gaussian error on  $H_0$ . Notice that the SN likelihood contours are estimated through the full likelihood function rather than with a Fisher matrix to facilitate the comparison with current estimates. We will compare the LSS forecasts also with the present SN dataset of Riess et al. (2004).

For the bias of the galaxy populations at  $z = 1$  and  $z = 3$  we adopt the same values as in SE, i.e.  $b \sim 1 – 1.5$  at  $z \sim 0.5 – 1$  and  $b \sim 3.3$  at  $z \approx 3$  (see Adelberger et al. 1998). Specifically, we assume  $\sigma_{8,m}(z = 0) = 0.9$  and  $\sigma_{8,m}(z) = \sigma_{8,m}(0)G(z)$  and  $\sigma_{8,g} = 1$  at  $z = 3$  and  $\sigma_{8,g} = 1.8$  at all other redshift bins.

## 4 PERFECT FLUID DARK ENERGY

To review notation and to check our code against the results of SE we begin the analysis with their DE model, based on a perfect fluid with equation of state  $p = w(z)\rho$  where

$$w(z) = w_0 + w_1 z. \quad (18)$$

Notice that such a perfect fluid model can be only a phenomenological description of the background dynamics at low  $z$ . Beside the obvious fact that  $w$  diverges at high  $z$ , the problem is that a meaningful derivation of the fluctuation equations requires as additional prescription the dependence of  $w$  on the perturbed dark energy density. Moreover, if one assumes for simplicity that  $\delta w/\delta\rho = 0$ , then dark energy becomes highly unstable at small scales since the sound speed  $c_s \equiv \sqrt{\delta p/\delta\rho}$  is imaginary for  $w(z) < 0$ . We can discuss therefore the growth function only in the  $\Lambda$ CDM limit  $w_0 = -1, w_1 = 0$ . In this limit a useful approximation is

$$\frac{d \log G}{d \log a} = \Omega_m(a)^\gamma, \quad (19)$$

with  $\gamma \approx 0.6$ . Since  $G$  can be calculated only in the  $\Lambda$ CDM limit, we assume that  $G$  does not depend on  $w_0, w_1$ : this is a conservative statement, since any dependence would further restrict the area of the confidence region. Moreover, we found that, naively extending the validity of (19) to other values of  $w_0, w_1$  (i.e. assuming dark energy to be completely homogeneous), the results do not change sensitively. Therefore  $G$  will be assumed in this section to depend only on  $\Omega_{m0}$ . The derivative with respect to  $\Omega_{m0}$  is

$$\frac{\partial \log G}{\partial \Omega_{m0}} = \gamma \int \Omega_m(\alpha)^\gamma \frac{d \log \Omega_m}{d \Omega_{m0}} d\alpha = -\gamma \int \frac{e^{3\alpha} \Omega_m(\alpha)^\gamma}{[e^{3\alpha}(\Omega_{m0} - 1) - \Omega_{m0}] \Omega_{m0}} d\alpha. \quad (20)$$

Once we have the total Fisher matrix we invert it and extract a submatrix  $F_{sub,ij}$  containing all the parameters  $p_i$  that depend on the cosmological parameters  $\omega_m, \Omega_{m0}, w_0, w_1$ . Beside  $\omega_m, \Omega_{m0}$  these are, *for each survey*,

$$\log D, \log H, \log G, \quad (21)$$

plus  $\log D$  for the CMB. The diagonal elements of  $F_{sub,ij}^{-1}$  give the square of the errors on the relative variables. The relative errors on  $H, D, G$  are plotted in Fig. 2 for the various surveys and redshift errors. These intermediate results are consistent with those given in SE (who however considered a different combination of surveys and volumes). As remarked in SE, the errors on  $D$  (contrary to  $H$  and  $G$ ) depend only weakly on redshift uncertainty. At  $z = 1$  the angular diameter distance can be estimated to 4.3 % in a spectroscopic survey of area 200 deg<sup>2</sup> and to 7.5%(10.0%) in a similar survey with  $\delta z = 0.02(0.04)$ . Roughly a factor of 2 is gained by extending to 1000 deg<sup>2</sup>.

Changing to the DE variables

$$d_n = (\Omega_{m0}h^2, \Omega_{m0}, w_0, w_1), \quad (22)$$

we obtain finally the projected DE Fisher matrix

$$F_{DE,mn} = \left( \frac{\partial p_i}{\partial d_m} \right) F_{sub,ij} \left( \frac{\partial p_j}{\partial d_n} \right). \quad (23)$$

Then we again invert and take a submatrix  $M_{w_0, w_1}$  whose eigenvalues and eigenvectors define the confidence ellipsoid on the plane  $w_0, w_1$ . Notice that a two-dimensional confidence region corresponding to  $1\sigma$  includes only 39% of likelihood. Here and in all subsequent plots the confidence regions are given to 68% : this requires therefore that the  $1\sigma$  values of the parameters (i.e. the eigenvalues of the two-dimensional Fisher submatrix) are multiplied by 1.51.

The results for the various surveys and for different redshift errors are in Figs. 3-6. In Fig. 3 and 4 we show the effect of marginalizing over  $G$  versus fixing  $G = G(\Omega_{m0})$  as in Eq. (19) for the four surveys at  $z \approx 1$  and the survey at  $z = 3$ , always including CMB and SDSS. As it can be seen, the effect is rather strong, especially at  $z = 3$ , where the information in  $G$  almost halves the errors in  $w_0, w_1$ . At this redshift, we could say that a survey of 200 deg<sup>2</sup> that includes the information in  $G$  (from now on, we call this approach “including  $G$ ”) is roughly equivalent in terms of constraining power to a survey of 1000 deg<sup>2</sup> with  $G$  marginalization (“marginalizing over  $G$ ”). The effect at  $z \approx 1$  is smaller, because  $\partial \log G / \partial \Omega_{m0}$  is smaller at low  $z$  (see Fig. 1).

In Fig. 5 we show the results for all redshift bins marginalizing over  $G$  as in SE while in Fig. 6 we include  $G(z)$ . In the same plots we show the contours of the likelihood for simulated SNIa data. These are obtained by a full likelihood analysis of simulated datasets, marginalizing over the Hubble parameter derived from the SNIa themselves. This renders SNIa sensitive to the slope  $d \log D_L / dz$  of the luminosity distance  $D_L$ , rather than to its absolute value. Since

$$\frac{d \log D_L}{dz} \propto \frac{1}{H(z) D_L(z)}, \quad (24)$$

it is clear that the SNIa data is nearly degenerated in the direction of  $HD = const$ , at  $z \approx 1$ . In Figs. 5-6 we also show the 68% confidence region for SNIa obtained assuming instead a 10% gaussian error in  $H_0$ .

The  $1\sigma$  errors on  $\omega_m, \Omega_m, w_0, w_1$  are reported in Table III and IV, where we include always  $G(z)$ . For  $\omega_m$  we give the relative errors; for the other parameters the absolute one. Let us consider first the *spectroscopic* results. In the best case (all redshift bins over an area of 1000 deg<sup>2</sup> survey) the errors on  $w_0$  and  $w_1$  are 0.12 and 0.16, respectively. Marginalizing over  $G$  we obtain 0.19 and 0.23: the information in  $G$  reduces the errors by roughly 30%. The error on  $\Omega_m$  goes from 0.017 including  $G$  to 0.03 marginalizing over  $G$ .

For the *photometric* case ( $\delta z = 0.02$ ) the best case of Table IV gives  $\sigma_{w_0} = 0.32$  and  $\sigma_{w_1} = 0.39$ . A hybrid survey could reduce the errors to 0.23 and 0.23, respectively. Reducing the density of the  $z \approx 1$  surveys leaves almost unaltered the constraints in the spectroscopic case (since the ratio  $nP/(1+nP)$  in Eq. (15) is already close to saturation) while weakens the photometric constraints by a few percent (see Table IV).

The relative error on the Hubble parameter  $h = (\omega_m / \Omega_{m0})^{1/2}$  is dominated by the relative error on  $\Omega_{m0}$  and is therefore approximated by  $\sigma_{\Omega_{m0}} / 2\Omega_{m0}$ . We find  $\Delta h / h \approx 3 - 7\%$ .

It is interesting to comment also on the inclusion of SNIa data. The supernovae constrain  $w_0$  to a much higher precision than  $w_1$ . Multiplying the baryon oscillations contours with the SN limits one sees that the advantage of spectroscopy reduces considerably, at least below 200 deg<sup>2</sup>, almost regardless of  $\delta z$ , as can be seen in Fig. 7.

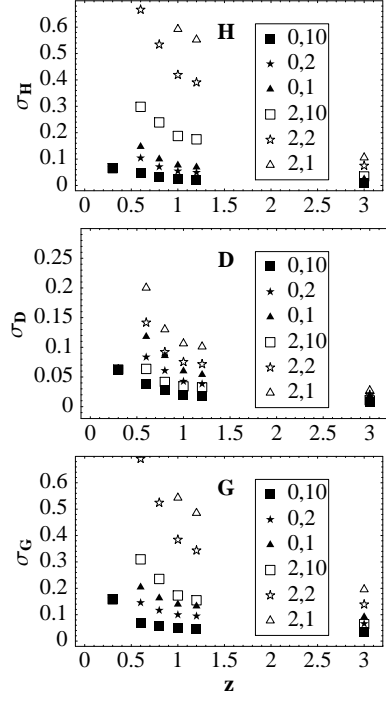
We compare our baryon oscillations forecasts also with the *present* SN data. In Fig. 8 we show the constraints from the current set of supernovae of Riess et al. (2004; *gold* sample), along with the constraints for a 200 deg<sup>2</sup> survey (marginalizing over  $G$ ) with reference cosmology centered on the Riess et al. (2004) best fit,  $w_0 \approx -1.3$ ,  $w_1 \approx 1.5$  and  $\Omega_{m0} = 0.27$ . This plot shows that the size and orientation of the Fisher contour regions depends in a significant way on the underlying reference cosmology, as already remarked in SE. It also reveals that, in cases as this, the spectroscopic surveys maintain their advantage even using the SN information.

Table III. Spectroscopic surveys

Area (deg <sup>2</sup> )	$\sigma_{\omega_m}$	$\sigma_{\Omega_m}$	$\sigma_{w_0}$	$\sigma_{w_1}$
$z = 1$				
100	0.0053	0.037	0.39	0.56
200	0.0053	0.033	0.34	0.48
1000	0.0052	0.024	0.22	0.31
$z = 3$				
100	0.0051	0.045	0.32	0.36
200	0.0050	0.043	0.31	0.33
1000	0.0041	0.037	0.25	0.25
all surveys				
100	0.0051	0.034	0.26	0.32
200	0.0049	0.029	0.21	0.26
1000	0.0040	0.017	0.12	0.16

Table IV. Photometric ( $\delta z = 0.02$ ) surveys

Area (deg <sup>2</sup> )	$\sigma_{\omega_m}$	$\sigma_{\Omega_m}$	$\sigma_{w_0}$	$\sigma_{w_1}$
$z = 1$				
100	0.0054	0.046	0.45	0.72
200	0.0054	0.046	0.42	0.63
1000	0.0053	0.043	0.35	0.45
$z = 3$				
100	0.0053	0.046	0.45	0.70
200	0.0053	0.046	0.42	0.62
1000	0.0052	0.045	0.35	0.45
all surveys				
100	0.0053	0.045	0.42	0.62
200	0.0053	0.044	0.39	0.54
1000	0.0050	0.039	0.32	0.39
hybrid surveys				
100	0.0052	0.044	0.31	0.34
200	0.0050	0.042	0.30	0.31
1000	0.0041	0.033	0.23	0.23
density/10 at $z \approx 1$				
100	0.0053	0.045	0.44	0.67
200	0.0053	0.045	0.41	0.59
1000	0.0051	0.040	0.34	0.42



**Figure 2.** Relative errors for  $H, D, G$  for the various surveys. The legend label  $x, y$  means a survey with redshift error  $x/100$  and area  $y \cdot 100 \text{ deg}^2$ . The dot at  $z = 0.3$  is the SDSS survey.

## 5 SCALAR FIELD MODEL

The perfect fluid DE model of the previous section is a useful toy model but has no theoretical motivation and is incomplete in the sense that it is only a description of the background dynamics at low redshifts. In this section we perform the analysis by considering an example of a microphysical description of DE based on a scalar field model.

We adopt to this purpose one of the first and simplest scalar field model proposed in literature, the inverse power-law potential (Ratra & Peebles 1988, Steinhardt et al. 1999)

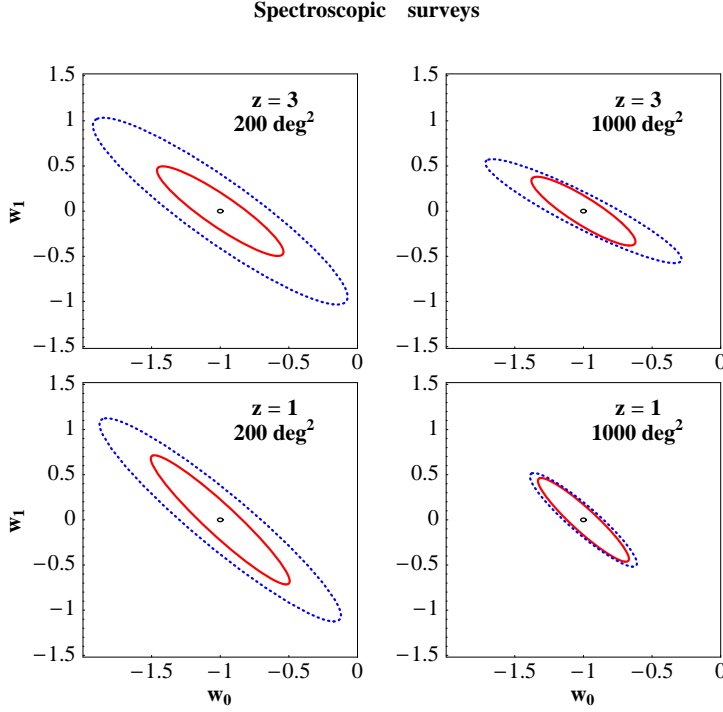


**Figure 3.** Effect of the growth function for spectroscopic surveys: confidence regions marginalizing over  $G$  (dotted curves) and using the information in  $G$  (full curves). The plots are for the survey at  $z = 3$  alone (upper panels) and for  $z = 1$  alone (lower panels). In the color version of the figures lines referring to  $G$ -marginalization are blue, those referring to the inclusion of  $G$  are in red.

$$V = A\phi^{-n}. \quad (25)$$

The cosmological equations for this model are conveniently written in the  $e$ -folding time  $\alpha = \log a = -\log(1+z)$  as (the prime denotes derivation with respect to  $\alpha$ )

$$\phi'' + \phi'(2 + \frac{H'}{H}) + a^2 V_{,\phi} = 0, \quad (26)$$

$$H^2 = H_0^2 \Omega_{m0} a^{-3} + \frac{\kappa^2}{3} \left( \frac{1}{2} \phi'^2 H^2 + V \right), \quad (27)$$

where  $\kappa^2 = 8\pi G$ ,  $H_0^{-1} = 3000 \text{Mpc}$ , and  $\Omega_{K,P}$  denote the kinetic and potential energy, respectively, of the scalar field. It is convenient to introduce the notation  $x^2 = \frac{\kappa^2 \phi'^2}{6} = \Omega_K$ ,

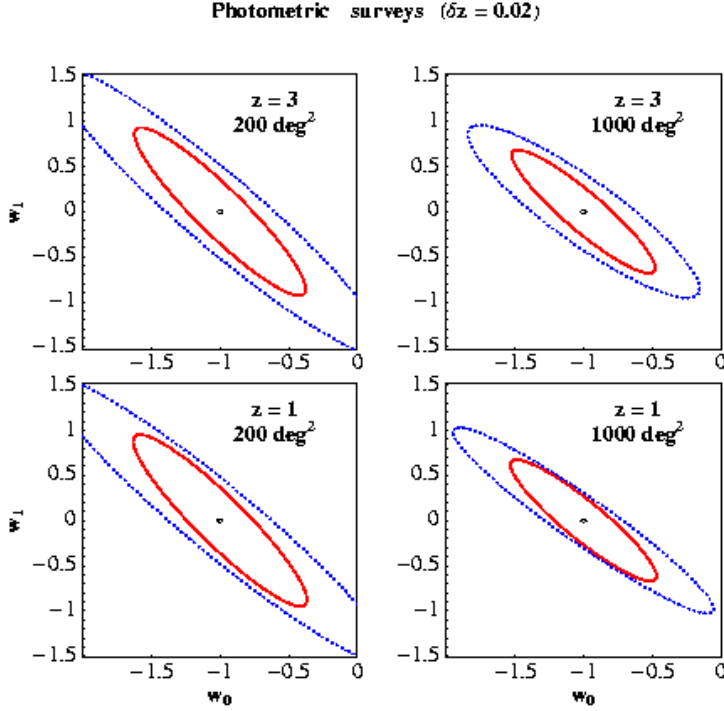


**Figure 4.** Effect of the growth function for photometric surveys: confidence regions marginalizing over  $G$  (dotted curves) and including  $G$  (full curves). The plots are for the survey at  $z = 3$  alone (upper panels) and for  $z = 1$  alone (lower panels).

$y^2 = \frac{\kappa^2 V}{3H^2} = \Omega_P$  and  $h = H/H_0$  (which should not be confused with the dimensionless Hubble parameter). Eq. (27) becomes then (Amendola 2000)

$$h^2 = \frac{\omega_{m0} a^{-3}}{1 - x^2 - y^2}. \quad (28)$$

Then the equations can be written as a dynamical system as

$$\begin{aligned} x' &= -\frac{3}{2}x(x^2 - y^2 - 1) - \mu y^{2(1+n)/n} h^{2/n}, \\ y' &= \mu x y^{(2+n)/n} h^{2/n} + \frac{3}{2}y(1 + x^2 - y^2), \\ h' &= -\frac{h}{2}(3 + 3x^2 - 3y^2), \end{aligned} \quad (29)$$

where we introduced the dimensionless quantity

$$\mu = -\frac{n}{\sqrt{2}} \left(\frac{\kappa^2}{3}\right)^{-\frac{n+2}{2n}} A^{-1/n} H_0^{2/n} = -n \sqrt{\frac{3}{2}} (\kappa \phi_0)^{-1} \Omega_{P0}^{-1/n},$$

where  $\phi_0$  is the present value of the scalar field and  $\Omega_{P0}$  its present potential density. The system can be solved numerically to derive  $x(z), y(z)$  for each value of the parameters  $n, \Omega_{m0}, \mu$

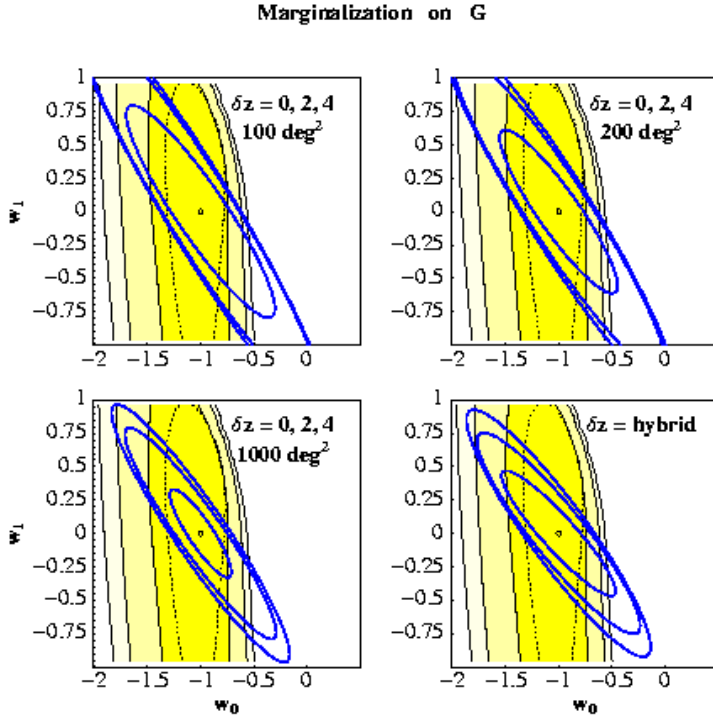


**Figure 5.** Confidence ellipsis for the combined data CMB,SDSS, surveys at  $z \approx 1, 3$ , for three redshift errors, 0, 0.02 and 0.04, inside to outside. Here and in all subsequent plots the redshift errors are indicated as  $100 \cdot \delta z$ . The central dot is the reference cosmology. The bottom right panel refers to the hybrid survey discussed in the text (spectroscopic plus photometric): here the contours are for surveys of 1000, 200 and 100  $\text{deg}^2$ , inside to outside. The shaded areas are the confidence regions for 400 simulated SNIa distributed according to the reference cosmology up to  $z = 1.5$ , at 68%, 95% and 99% c.l., inside to outside, marginalizing over  $H_0$  (uniform prior) and over  $\Omega_{m0}$  with a Gaussian centered on the reference value and variance 0.1. The dotted contour (at 68% c.l.) assumes instead a 10% Gaussian error on  $H_0$  for the SNIa.

but this is computationally cumbersome and hides interesting features of the solutions. In Steinhardt et al. (1999) it has been shown in fact that such a model possesses a tracking solution, defined as a trajectory on which many initial conditions converge, as shown in Fig. 9. Once a solution reaches this trajectory its properties are determined solely by the slope  $n$  and the present value  $\Omega_{m0}$ . As long as  $x, y \ll 1$  the tracking trajectory has  $w_\phi \approx -2/(2+n)$ ; when later on DE takes over,  $y$  tends to unity and  $w_\phi \rightarrow -1$ . Since the variation of  $w_\phi$  is relatively small, to a first approximation the inverse power-law model for  $n \ll 1$  resembles a perfect fluid with  $w_0 \approx -2/(2+n)$  and  $w_1 \approx 0$ .

In the Appendix we derive a semi-analytical fast approximation to the tracking trajectory that interpolates correctly between the two limits of  $w_\phi$ . This approximation will be used in

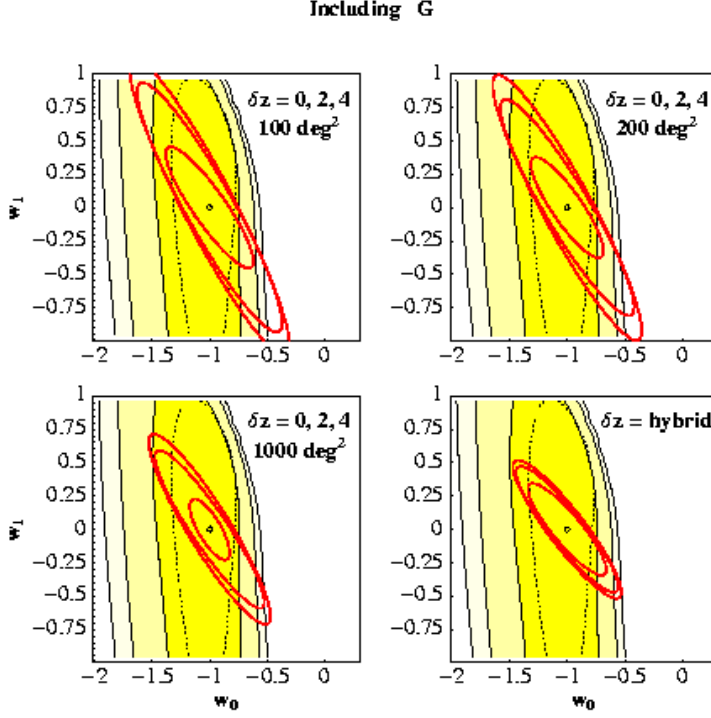


**Figure 6.** As in Fig. 5 but including the dependence of the growth factor  $G$  on the DE parameters.

what follows; it is found to be precise to better than 1% on  $\Omega_m(z)$  and to better than 5% on  $w_\phi(z)$  across all the relevant range. Further, we find that for the growth function the same approximation  $d \log G(z)/d\alpha = \Omega_m^\gamma(\alpha)$  adopted for  $\Lambda$ CDM remains valid, with deviation from the numerical result less than 0.1% in the range  $z \in (0, 3)$  putting  $\gamma = 0.575$  for  $n \approx 0$  and  $\gamma = 0.625$  for  $n \approx 0.5$ . For all practical purposes the dependence of  $\gamma$  on  $n$  can be neglected and we put  $\gamma = 0.6$  in the whole interesting range.

We project now the Fisher matrix in the subspace

$$d_n = (\Omega_{m0}h^2, \Omega_{m0}, n). \quad (30)$$

The results are shown in Fig. 10 (reference cosmology  $n = 0.05$ , practically indistinguishable from  $\Lambda$ CDM) projected on the plane  $\Omega_{m0}, n$ , and in Table V. As expected, the SN contours are elongated towards the contours of  $HD$  (see the contour plots in Fig. 11). The contours of the Fisher matrix are instead slanted towards the direction of the iso- $G$

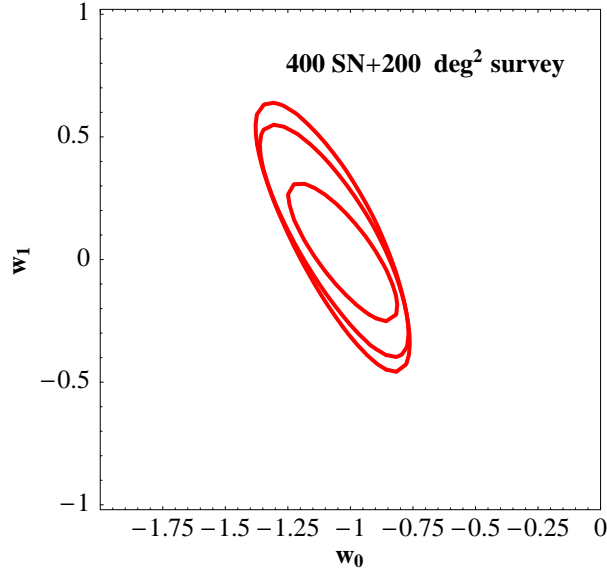


**Figure 7.** Contours at 68% of the combined likelihood of supernovae and surveys of  $200 \text{ deg}^2$  with redshift errors  $\delta z = 0, 0.02, 0.04$ , inside to outside (including  $G$ ).

lines: this shows that it is the information in  $G$  that drives the results. This optimizes the complementarity between SNIa and LSS.

The tracking scalar field model has been tested towards SNIa and CMB. We analysed the recent Riess et al. (2004) SNIa data with the inverse power-law potential and found the constraint  $n < 0.9$  at 68% c.l. ( $n < 0.5$  assuming  $\Omega_{m0} = 0.3 \pm 0.05$ ). On the other hand WMAP data allow for  $n < 0.94$  (or  $n < 0.74$  including the HST prior on the Hubble constant), at 68% c.l (Amendola & Quercellini 2003). From Fig. 10 and Table V we see that the baryon oscillations for a scalar field model can constrain  $\Omega_{m0}$  to within 0.01 to 0.03, and the slope  $n$  to  $n < 0.15$  and  $n < 0.53$ , depending on the survey strategy. In all cases this is quite better than the current and near-term SN and CMB constraint. Once again, most of the advantage of spectroscopic measures vanishes if one takes into account the SNIa contours (see Fig. 12)

Here again we perform the comparison with the Riess et al. (2004) *gold* sample of supernovae (Fig. 13). It can be seen that the present SN data already cut most of the vertical elongation of the contours for the photometric surveys, leading to constraints on  $n$  which are similar to those from spectroscopic surveys. The spectroscopic errors on  $\Omega_{m0}$  remain however competitive.

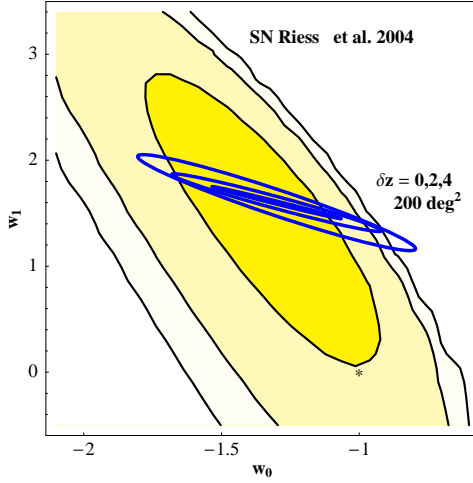


**Figure 8.** Here we compare the confidence regions of  $200\text{deg}^2$  surveys with redshift errors of 0, 0.02 and 0.04 (marginalized over  $G$ ) to the recent SN data of Riess et al. (2004) assuming  $\Omega_{m0} = 0.27 \pm 0.04$  (Gaussian errors). For this plot the reference cosmology in the Fisher matrix coincides with the best fit to the SN ( $w_0 = -1.3, w_1 = -1.5$ ) . The SN contours are 68,90 and 95% . The star marks the  $\Lambda\text{CDM}$  model.

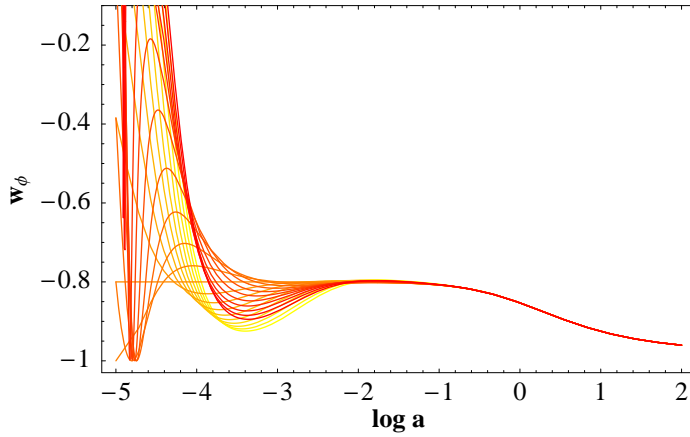


**Figure 9.** Equation of state of the scalar field model for several different initial conditions. The plot shows the tracking behavior: all curves converge to a trajectory which, at early times, has constant equation of state  $w_\phi \approx -\frac{2}{2+n}$  and asymptotically converge to  $w_\phi = -1$ . Here  $n = 0.5$  and  $\Omega_{m0} = 0.35$ .

## 6 CONCLUSIONS

Future deep and wide redshift surveys will have the chance to explore the little known landscape at  $z \approx 1 - 3$  between the recent and early universe. This is the epoch at which dark energy begins to impel its thrust to the expansion: it is therefore of extreme interest for cosmology in order to gain hold of reliable data on its evolution. As it has been shown by the recent releases of high redshift SN data (Tonry et al. 2003, Riess et al. 2004) the use of standard candles will have much to improve before it will be able to set stringent limits on the dark energy equation of state evolution. Moreover, there are still no solid proposals for standard candles visible at redshifts significantly higher than  $z \approx 1.5$ . Other probes of the expansion dynamics at larger distances (gamma-ray bursts, lensing) might be promising but depend on unknown physics and modeling.

The use of the baryon oscillations in the matter power spectrum is on the contrary based on well-known phenomena that have already seen a spectacular validation in CMB observations. Moreover, it can provide a tomography of the universe expansion from  $z = 0$  down to  $z \approx 3.5$ , virtually without loss of precision. An intrinsic advantage of this method is the combined use of  $H$ ,  $D$  and  $G$  to reduce the degeneracies of each of these quantity. We have shown that the inclusion of  $G$  reduce the errors by 30% roughly. We found that a  $200^2$  survey with absolute redshift error of  $\delta z = 0.02$  can limit  $w_0, w_1$  by 0.39 and 0.54, respectively, assuming  $w_0 = -1, w_1 = 0$  as reference values. A spectroscopic survey can reduce the uncertainties to 0.21 and 0.26. If the dark energy is modeled as a scalar field with inverse power-law potential  $n$ , the limits are  $n < 0.26$  (spectroscopic redshift) and  $n < 0.40$  (redshift error  $\delta z = 0.02$ ), along with an estimation of  $\Omega_{m0}$  to better than 3%. Inclusion of supernovae data further reduce the errorbars due to the different direction of degeneracy. The reduction is found to be particularly efficient in the case of photometric redshift measurements.

## REFERENCES

Adelberger K.L. et al. 1998, ApJ, 505, 18  
 Amendola L. & Quercellini C., 2003, Phys. Rev. D68, 023514  
 Amendola L., 2000, Phys. Rev. D62, 043511, astro-ph/9908440  
 Bassett B. & Kunz M., 2003, astro-ph/0311495, ApJ in press  
 Bennet C. et al, 2003, Ap. J. 583, 1-23, astro-ph/0301158  
 Blake C. & Glazebrook K., 2003, ApJ, 594, 665, astro-ph/0301632  
 Cooray A, Huterer D. & Baumann D., 2004, Phys. Rev. D69, 027301  
 Eisenstein D.L , Hu W. & Tegmark M., 1999 ApJ 518, 2  
 Eisenstein D.J. et al. 2001, AJ 122, 2267  
 Halverson N. W. et al., 2002 Ap.J. 568, 38, astro-ph/0104489  
 Lee A.T. et al., 2001 Ap.J. 561, L1 astro-ph/0104459  
 Linder, E. V. 2003, 2003, Phys. Rev. D 68, 083504  
 Netterfield C. B. et al., 2002 Ap.J. 571, 604, astro-ph/0104460  
 Peacock J. A. & West M.J. 1992, MNRAS, 259, 494  
 Pedichini F. et al. 2003, SPIE, 4841, 815

Perlmutter S. et al. 1999 Ap.J., 517, 565  
 Poli F., Menci N., Giallongo E., Fontana A., Cristiani S. & D'Odorico S., 2001, ApJ, 551, L45 (erratum 551, L127)  
 Poli F. et al. 2003, ApJ, 593, L1  
 Ratra B. & P.J.E. Peebles, 1988, Phys. Rev. D37, 3406  
 Riess A.G. et al. 1998, A.J., 116, 1009  
 Riess A. G. et al. 2004 astro-ph/0402512  
 Seljak U. 1996 ApJ 482, 6  
 Seljak U. and M. Zaldarriaga, 1996, Ap.J., 469, 437  
 Seo H.J. & Eisenstein D., 2003, astro-ph/0307460  
 Soucail G. ,Kneib J.-P. and Golse G., 2004, astro-ph/0402658  
 Steidel C.C., Adelberger K.L., Dickinson M., Giavalisco M., Pettini, M. & Kellogg M. 1998, ApJ, 492, 428  
 Steinhardt P.J., L. Wang & I. Zlatev, 1999, Phys. Rev. D59, 123504  
 Tegmark M. 1997, Phys. Rev. Lett. 79 3806  
 Tonry J.T. et al. 2003, Ap.J. 594,1  
 Wolf, C., Meisenheimer, K., & Roser, H.-J. 2001, A&A, 365, 660

## APPENDIX. THE FAST-TRACK APPROXIMATION

A tracking solution, as any other trajectory, is defined in a 3D phase space by two relations of the form  $e_{1,2} = f_{1,2}(x, y, h)$  where  $e_{1,2}$  are constants. There must exist therefore two constants of motion of the system (29). In the original derivation of the tracking solution (Steinhardt et al. 1999) it was found that the equation of state

$$w = \frac{x^2 - y^2}{x^2 + y^2}, \quad (31)$$

is almost constant during the tracking. The second constant of motion is

$$q = y^{(2+n)/n} h^{2/n}. \quad (32)$$

Then, by derivating, we obtain for the tracking solution

$$\begin{aligned} q_t &= -\frac{3}{2\mu} \sqrt{1 - w^2}, \\ w_t &= \frac{2 - 2n + x^2 - y^2}{2n - 1}. \end{aligned} \quad (33)$$

The second relation says that  $w, q$  are constant only for  $x^2 - y^2 \ll 1$ : this is the regime in which the tracking behavior was originally found. In this case

$$w = -\frac{2}{2 + n}. \quad (34)$$

However, since near the present epoch  $x^2, y^2$  are no longer negligible, it is necessary to improve the accuracy over the solution (34). Substituting  $w$  from Eq. (31) in (33) we obtain (assuming  $w > -1$ )

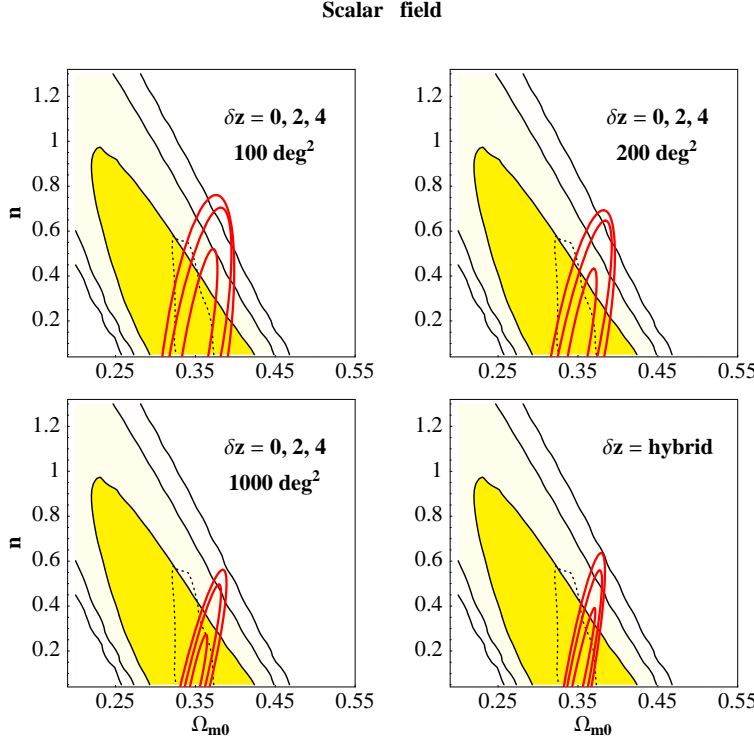


**Figure 10.** As in Fig. 5 but for the scalar field model. Here the SNIa confidence regions are not marginalized over  $\Omega_{m0}$ .

$$w(y, n) = \frac{1 - 2y^2 - \sqrt{9 - 24(1+n)/n + 16(1+n)^2/n^2 - 4y^2 + 4y^4}}{4/n + 2}. \quad (35)$$

From (32) we obtain

$$y = (qh^{2/n})^{\frac{n}{2+n}}. \quad (36)$$

Employing (28) we obtain finally

$$y = \left[ -\frac{3}{2\mu} \sqrt{1 - w(y, n)^2} \left( \frac{\omega_m a^{-3}}{1 - y^2(\frac{2}{1-w(y,n)})} \right)^{2/n} \right]^{\frac{n}{n+2}}. \quad (37)$$

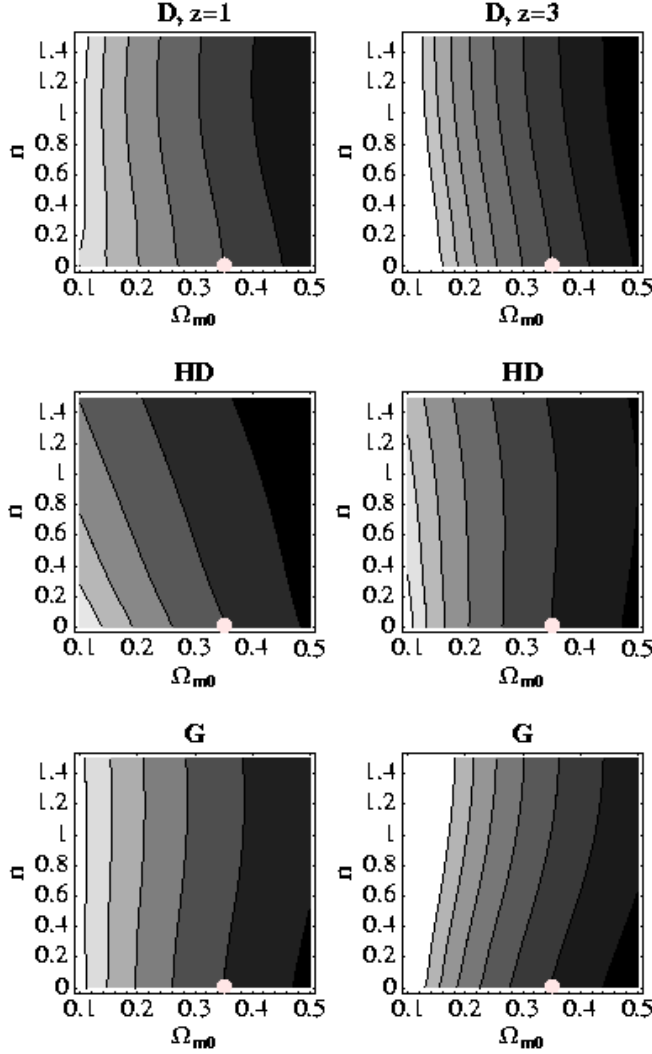


**Figure 11.** The plot displays the contours of  $D, HD, G$  at  $z = 1$  (left column) and  $z = 3$  (right column). Each function is normalized by the value at the reference cosmology, marked by the white dot. The contours are for steps of 0.05, increasing from black to white

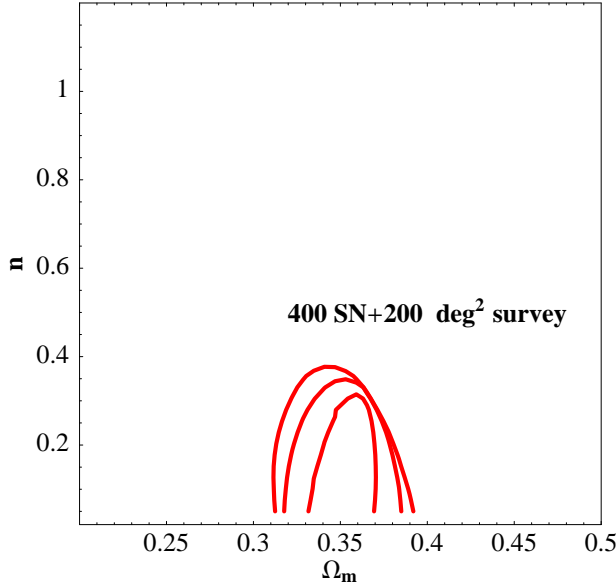


**Figure 12.** Scalar field: contours at 68% of the combined likelihood of supernovae and surveys of 200 deg<sup>2</sup> with redshift errors  $\delta z = 0, 0.02, 0.04$ , inside to outside (including  $G$ ).

The parameter  $\mu$  has to be fixed so that at the present  $y^2 + x^2 = 1 - \Omega_{m0}$ . This gives a relation  $\mu = \mu(n, \Omega_{m0})$ . We found by iterative integrations that a very good fit to  $\mu$  is

$$\mu = \exp[-0.53 - \frac{0.00036}{n^3} + \frac{0.0033 + 0.0088\Omega_{m0}}{n^2} - \frac{0.13 - 1.16\Omega_{m0} + 0.41\Omega_{m0}^2 - 1.69\Omega_{m0}^3}{n} + 0.31n + 2.43\Omega_{m0} - 1.25\Omega_{m0}^2].$$

With this substitution, Eq. (37) becomes an implicit algebraic relation that, solved numerically for  $y$ , gives  $y(a; n, \Omega_{m0})$  and all related quantities  $(x(t), w(t), h(t))$ .

Table V. Results for scalar field.

Area (deg <sup>2</sup> )	$\sigma_{\omega_m}$	$\sigma_{\Omega_m}$	$\sigma_n$
$\delta z = 0$			
100	0.0032	0.018	0.32
200	0.030	0.016	0.26
1000	0.0022	0.010	0.15
$\delta z = 0.02$			
100	0.0034	0.030	0.44
200	0.0033	0.028	0.40
1000	0.0031	0.021	0.30
$\delta z = 0.04$			
100	0.0034	0.032	0.47
200	0.0034	0.030	0.43
1000	0.0033	0.026	0.34
hybrid surveys			
100	0.0032	0.023	0.39
200	0.0031	0.020	0.34
1000	0.0026	0.014	0.23

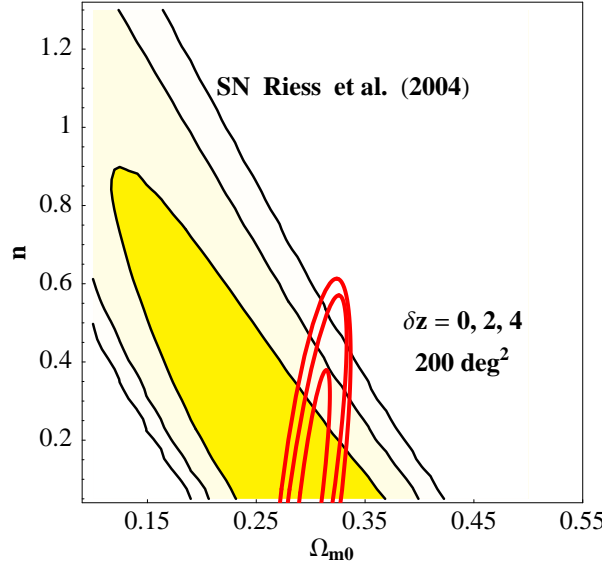


**Figure 13.** Here we compare the confidence ellipsis of  $200\text{deg}^2$  surveys with absolute redshift errors of  $\delta z = 0, 0.02$  and  $0.04$  (inside to outside), with the confidence regions for the scalar field model with the SN data of Riess et al. (2004) For this plot the reference cosmology in the Fisher matrix coincides with the best fit to the SN ( $\Omega_{m0} = 0.3, n = 0$ ). The SN contours are 68,90 and 95% .